Modulating negative magnetoresistance via inducing vacancy for regulates electron transport under magnetic ambient conditions

Meng Li, Jingxue Sun [*], Xin Zhou, Huaisuo Yao, Bowen Cong, Yingxuan Li, Gang Chen

MIIT Key Laboratory of Critical Materials Technology for New Energy Conversion and Storage, School of Chemistry and Chemical Engineering, Harbin Institute of Technology, Harbin 150001, PR China

ARTICLE INFO

ABSTRACT

The introduction of external magnetic field is one of the most widely studied strategies for photogenerated carrier separation in recent years. However, magnetic materials have great disadvantages in terms of photocatalytic performance. Semiconductor materials with magnetic properties are also extremely rare. It is extremely peculiar to research the magnetism of semiconductor photocatalyst triggered by vacancy. Here, the first example of ferromagnetic Bi_2S_3 is achieved by controlled Bi vacancy (Bi_2S_3-V_{Bi}). The magnetism properties depends largely on the spin polarization of p electrons in S atoms, and its magnetic moment is mainly distributed on S atoms around cation vacancies. Under the induction of external magnetic field, the tunneling of spin-polarized electrons in S-2p orbital makes Bi_2S_3-V_{Bi} have negative magnetoresistance effect. The ferromagnetic arrangement of Bi_2S_3-V_{Bi} particles can reduce the resistivity and increase the tunneling of electrons. Meanwhile, Lorentz force generated by external magnetic field acts reversely on photogenerated electrons and holes, thus effectively inhibiting the recombination of carriers in photocatalyst. Moreover, the influence of Bi vacancy on Bi_2S_3 magnetism is investigated by DFT calculation. This study provides a new strategy for effective carrier separation in photocatalysis.

1. Introduction

The increasing demand for energy utilization makes mankind fall into a series of energy crisis and environmental pollution problems [1–3]. Semiconductor photocatalytic technology is one of the most promising technologies to solve environmental problems and energy crisis [4–6]. Cadmium sulfide (CdS) has attracted wide attention in the fields of photocatalytic hydrogen production and degradation due to its narrow band gap and suitable band structure [7–9]. Nevertheless, CdS is prone to photo-corrosion, photo-generated charge-hole recombination, which hinders the improvement of its photocatalytic efficiency [10,11]. Therefore, researchers solve the above problems by doping, introducing defects and constructing heterojunctions, etc. [12–14]. Chava et al. synthesized one-dimensional CdS nanorods containing S vacancies by low-temperature heating strategy. The introduction of S vacancies enhances the absorption of visible light. Meanwhile, it also acts as traps to prevent recombination of carriers [15]. However, these strategies to promote carrier separation are influenced by the inherent properties of photocatalysts [16,17]. Therefore, it is necessary to suppress the recombination of carriers by introducing external driving force.

Up to now, many research results demonstrate that electric field, microwave, piezoelectric, pyroelectric, magnetic field and other external fields have the ability to improve the charge separation of semiconductors [18–21]. Li et al. prepared α-Fe_2O_3/rGO nanocomposites by simple hydrothermal method, in which the interface between α-Fe_2O_3 and rGO is constructed. Under the action of external magnetic field, ferromagnetic Fe_2O_3 has negative magnetoresistance effect. The carriers can easily transfer from α-Fe_2O_3 to rGO through the interface, thus greatly promoting the photocatalytic activity [22]. However, magnetic Fe_2O_3 is rarely used in photocatalytic reactions, only serves as an electron transport platform.

Magnetoresistance (MR) effect is a spintronic phenomenon, in which the resistance value of metal or semiconductor changes with the applied magnetic field [23,24]. Negative magnetoresistance means that with the increase of external magnetic field intensity, the current increases and the resistance decreases through the material. So that more photogenerated carriers can be quickly transmitted to the surface and participate in photocatalytic reaction. The realization of photocatalytic reaction requires semiconductor materials, but the negative magnetoresistance effect usually appears in ferromagnetic materials. Therefore,

---

in order to make Bi_2S_3 semiconductor photocatalyst ferromagnetic, in this work, Bi_2S_3 is induced to spin split by introducing Bi vacancy. It is mainly due to the spin polarization of p electrons in S atoms, which leads to the magnetic moment of the system. Under the action of external magnetic field, the tunneling of spin-polarized electrons in S-2p orbital makes Bi_2S_3-V_{Bi} showing negative magnetoresistance effect, so that more electrons engage in the photocatalytic hydrogen evolution reaction. Meanwhile, the Lorentz force can act on the electrons and holes in the opposite direction. Therefore, this is conducive to the effective separation of electrons and holes. This work provides a reasonable means for introducing external field into photocatalytic system.

2. Experimental

2.1. Materials

Cadmium chloride pentahydrate ($CdCl_2 \cdot 5H_2O$), bismuth nitrate pentahydrate ($Bi(NO_3)_3 \cdot 5H_2O$), thiourea, sodium sulfite (Na_2SO_3), sodium sulfide nonahydrate ($Na_2S \cdot 9H_2O$), L-cysteine, ethylene glycol and ethylenediamine were bought from Aladdin Chemical Co., Ltd. Permanent magnet was bought from manganese magnetic metal technology Co., Ltd.

2.2. Solvothermal synthesis of CdS nanorods

4.17 mmol $CdCl_2 \cdot 5H_2O$ and 12.5 mmol thiourea were added to 35 mL of ethylenediamine. After 30 min of ultrasound, the reaction solution was transferred to a 50 mL Teflon-line stainless steel autoclave at 140 ℃ for 36 h. After the reaction, the precipitate was centrifuged and washed alternately with ethanol and distilled water for three times. The treated solid was placed in a 60 ℃ vacuum drying oven for drying.

2.3. Solvothermal synthesis of CdS/Bi₂S₃ and CdS/Bi₂S₃-V_Bi composite

The above 0.1 g CdS nanorod powder and 2.5 mmol L-cysteine were added to 12.5 mL ethylene glycol, and dispersed by ultrasonic for 30 min. Meanwhile, 2.5 mmol $Bi(NO_3)_3 \cdot 5H_2O$ and 2.5 mmol $Na_2S \cdot 9H_2O$ were added into 12.5 mL of ethylene glycol and stirred for 30 min. All the above solutions were transferred to 50 mL Teflon-line stainless steel autoclave at 160 ℃ for 12 h. The precipitate was centrifuged and washed three times alternately with water and ethanol. The solid was placed in a 60 ℃ vacuum drying oven overnight. The above sample was named as CdS/Bi_2S_3-V_{Bi}. When the amount of $Na_2S \cdot 9H_2O$ was 1.5 mmol, the sample was named as CdS/Bi_2S_3.

2.4. Characterizations

The micro-morphology of the samples was characterized by transmission electron microscope (TEM) and high resolution TEM (HRTEM, FEI Tecnai G2 S-Twin). X-ray diffraction (XRD, rigaku D/max-2000 diffractometer) was used to analyze the phase structure and composition of the samples. The elemental and valence states of the samples were determined by X-ray photoelectron spectroscopy (XPS, Thermo Scientific ESCALAB 250Xi). The UV–vis spectrum of samples was measured by spectrophotometer (HITACHI UH-4150). The photoluminescence (PL) spectrum were acquired based on spectrofluorometer (HORIBA FluoroMax-4). The magnetoresistance characteristics were determined by PPMS Dynacool-14T.

2.5. Photocatalytic hydrogen evolution test

20 mg photocatalyst powder and 30 μL terpineol were fully ground and then evenly spin-coated on 2 × 2 cm conductive glass. Subsequently, it was placed in a vacuum drying oven at 80 ℃ overnight. 1.0 M of sacrificial agent ($Na_2S + Na_2SO_3$) were added to 45 mL of distilled water and stirred until dissolved. The conductive glass loaded with the

photocatalyst was slowly placed into the photocatalytic reactor. In order to introduce magnetic field, the permanent magnet was placed under the photocatalytic reactor. Xenon lamp of 300 W (CEL-HXF300) was used as the light source of photocatalytic reaction. The content of hydrogen was automatically detected by gas chromatograph (Agilent 780A GC).

2.6. Density functional theory (DFT) calculation

Density functional theory (DFT) calculations were carried out by the Vienna ab initio simulation package (VASP), using the planewave basis with energy cutoff of 400 eV, projector augmented wave (PAW) potentials, and the PBE functional for the exchange-correlation energy. A k-point sampling of (3 × 1 × 1) grid was used to optimize the geometry structure, K is 3 × 3 × 3 of Gamma point symmetry, ENCUT = 400, the energy convergence standard was 0.00001 eV, and the force convergence standard was − 0.03 eV/A.

3. Results and discussion

3.1. Morphology and structure characterization

The schematic diagram of synthesizing CdS/Bi_2S_3-V_{Bi} composite photocatalyst by solvothermal method is shown in Fig. 1a. The morphology and structure of CdS/Bi_2S_3-V_{Bi} composite are characterized by SEM (Fig. 1b) and TEM (Fig. 1c). SEM and TEM images show that the average diameter and length of CdS nanorods are about 50 nm and 500–600 nm. Bi_2S_3-V_{Bi} nanoparticles with a size of about 40–50 nm are deposited on the surface of CdS nanorods. Meanwhile, Fig. S1 shows the micro-morphology of CdS/Bi_2S_3 nanocomposite. Fig. 1d clearly demonstrates the inseparable and successive interface formed between CdS and Bi_2S_3-V_{Bi}. This compact heterojunction structure facilitates electron transfer and transmit. Moreover, HRTEM further reveals that the lattice spacing of 0.33 nm corresponds to the (002) plane of the CdS phase, while 0.56 nm is classified as the (020) lattice plane of Bi_2S_3-V_{Bi}. The existence of Bi vacancy increases the lattice spacing of Bi_2S_3 from 0.54 nm to 0.56 nm (Fig. S2a). As shown in Fig. 1e, the crystal structures of CdS, Bi_2S_3, CdS/Bi_2S_3 and CdS/Bi_2S_3-V_{Bi} are characterized by XRD. The XRD peaks are consistent with standard CdS (PDF#47-1179, orthorhombic) and Bi_2S_3 (PDF#17-0320, orthorhombic) [25–27], which indicates that the existence of Bi vacancy does not change the phase structure of Bi_2S_3. Fig. 1f,g Fourier transform the HRTEM images to more evidently display the lattice fringes in CdS phase and Bi_2S_3-V_{Bi} phase. It can more intuitively show the lattice strain distribution induced by the existence of Bi vacancies. However, the HRTEM lattice FFT image of Bi_2S_3 shows no obvious lattice strain (Fig. S2b). Selected region electron diffraction (SAED) clearly shows the diffraction rings of the two phases, (220), (020) and (100) crystal plane can be attributed to CdS and Bi_2S_3-V_{Bi} respectively (Fig. 1h). Furthermore, the obvious diffraction ring fringes represent the polycrystalline characteristics of CdS/Bi_2S_3-V_{Bi} heterojunction samples. The EDX mapping demonstrate that Bi elements are distributed in the external region of CdS nanorods (Fig. 1h-m).

The chemical composition of CdS/Bi_2S_3 and CdS/Bi_2S_3-V_{Bi} are investigated by XPS spectroscopy [28]. The full spectrum of XPS shows that CdS/Bi_2S_3 and CdS/Bi_2S_3-V_{Bi} complex are composed of Cd, S, Bi, C and O elements (Fig. 2a). The illustration displays that CdS and Bi_2S_3 form heterojunction structure by sharing the S layer. In Fig. 2b, Cd^{2+} in CdS is evidenced by the doublet Cd $3d_{5/2}$ (404.6 eV) and Cd $3d_{3/2}$ (411.4 eV) [29–31]. Fig. 2c shows that 157.8 eV and 163.1 eV correspond to Bi $4f_{7/2}$ and Bi $4f_{5/2}$, while 160.8 eV and 161.5 eV commensurate with S $2p_{3/2}$ and S $2p_{1/2}$ [32–34]. Compared with S 2p and Bi 4f in CdS/Bi_2S_3, the binding energy of CdS/Bi_2S_3-V_{Bi} moves in a lower binding energy. This phenomenon is mainly attributed to the increase of electron density around Bi vacancies, which leads to the decrease of S^{2-} binding energy. This result further proves that there are abundant Bi vacancies in Bi_2S_3. The presence of Bi vacancies leads to the formation of
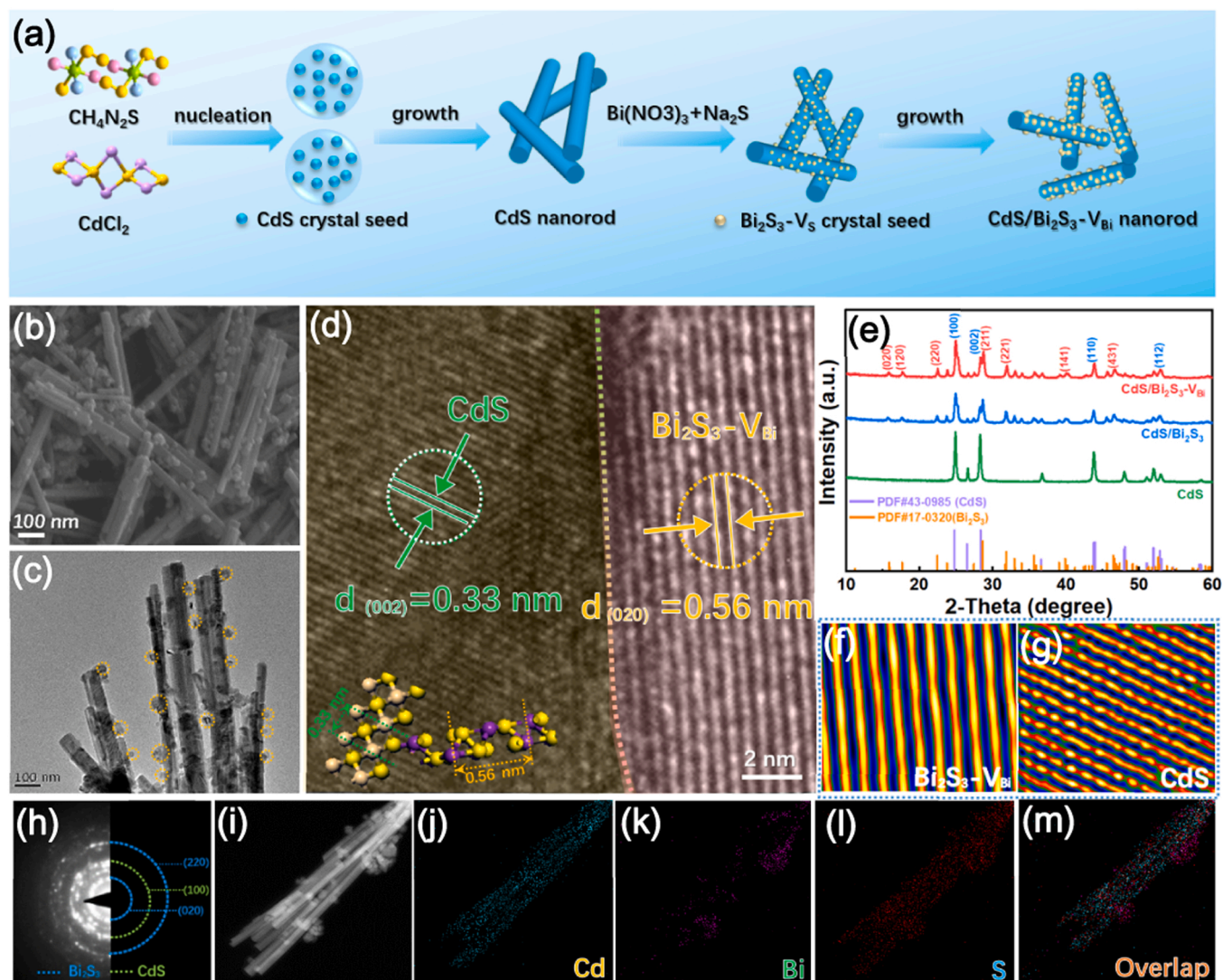
Fig. 1. (a) Schematic diagram of synthesis of CdS/Bi$_2$S$_3$-V$_{Bi}$ composite photocatalyst. (b) SEM image, (c) TEM image and (d) High resolution TEM (HRTEM) of CdS/Bi$_2$S$_3$-V$_{Bi}$ sample. (e) XRD patterns. (f) SAED patterns of CdS/Bi$_2$S$_3$-V$_{Bi}$. Fourier transformation images of (g) CdS and (h) Bi$_2$S$_3$-V$_{Bi}$. (i–l) EDX element mapping of CdS/Bi$_2$S$_3$-V$_{Bi}$ composite.

hanging S bonds, which can accommodate electrons. Therefore, CdS/Bi$_2$S$_3$-V$_{Bi}$ presents a more negative Zeta potential. As shown in Fig. S3, CdS/Bi$_2$S$_3$-V$_{Bi}$ (− 28.4 mV) has a more negative Zeta potential than CdS/Bi$_2$S$_3$ (− 13.6 mV). Therefore, the existence of Bi vacancy can be proved. In addition, the atomic ratios of CdS/Bi$_2$S$_3$ and CdS/Bi$_2$S$_3$-V$_{Bi}$ are quantitatively analyzed by ICP-MS. The atomic ratio of Cd:Bi:S in CdS/Bi$_2$S$_3$ is 0.23:0.56:1.08, the atomic ratio of CdS/Bi$_2$S$_3$-V$_S$ is 0.28:0.20:1.13. It is found that the atomic ratio of Bi element decrease more obviously (Table S1). In addition, the peak area of Bi element in CdS/Bi$_2$S$_3$-V$_{Bi}$ is smaller than that in CdS/Bi$_2$S$_3$, which further indicates that there are Bi vacancies in Bi$_2$S$_3$ lattice structure. Moreover, based on the XPS, the valence band (VB) of CdS 1.92 eV and that of Bi$_2$S$_3$ is 0.84 eV (Fig. S4). Nitrogen adsorption-desorption isotherm and pore size distribution of CdS/Bi$_2$S$_3$ and CdS/Bi$_2$S$_3$-V$_{Bi}$ are shown in Fig. 2d. The specific surface areas of CdS/Bi$_2$S$_3$ and CdS/Bi$_2$S$_3$-V$_{Bi}$ are 31.52 m^2 g^{-1} and 38.01 m^2 g^{-1}, respectively. The pore size distribution diagram demonstrates that both samples are mesoporous materials. The large specific surface area of CdS/Bi$_2$S$_3$-V$_{Bi}$ provides more active centers for the photocatalytic reaction, thus improving the photocatalytic performance.

3.2. Characterization of magnetic field effect

As shown in Fig. 3a, according to the left-hand rule, moving electrons and holes will be subjected to Lorentz force perpendicular to their moving direction in the magnetic field [35]. This causes electrons and holes to shift in opposite directions. Lorentz force suppresses the recombination of photogenerated carriers, so that more electrons can participate in photocatalytic reaction. Based on the theory of gradient drift and curve drift of magnetic field, Fig. 3b,c shows the trajectory of charge in magnetic field [36]. Assuming that there is no other external force, the movement of electrons in a uniform magnetic field is Larmor rotation. The center of its trajectory is also called the "guidance center", at which time the guidance center is stationary. The whole process of an electron moving in a magnetic field is shown in Video S1. When atoms absorb light, electrons that are originally in a smaller area gain energy. Under the action of Lorentz force, the distance between electron and nucleus increases, and the electron is more susceptible to the influence of magnetic field. The motion of electrons is affected by Lorentz force, which makes them unable to move to infinity. Electrons leaving the nucleus in certain directions are blocked back to the nucleus in short time.

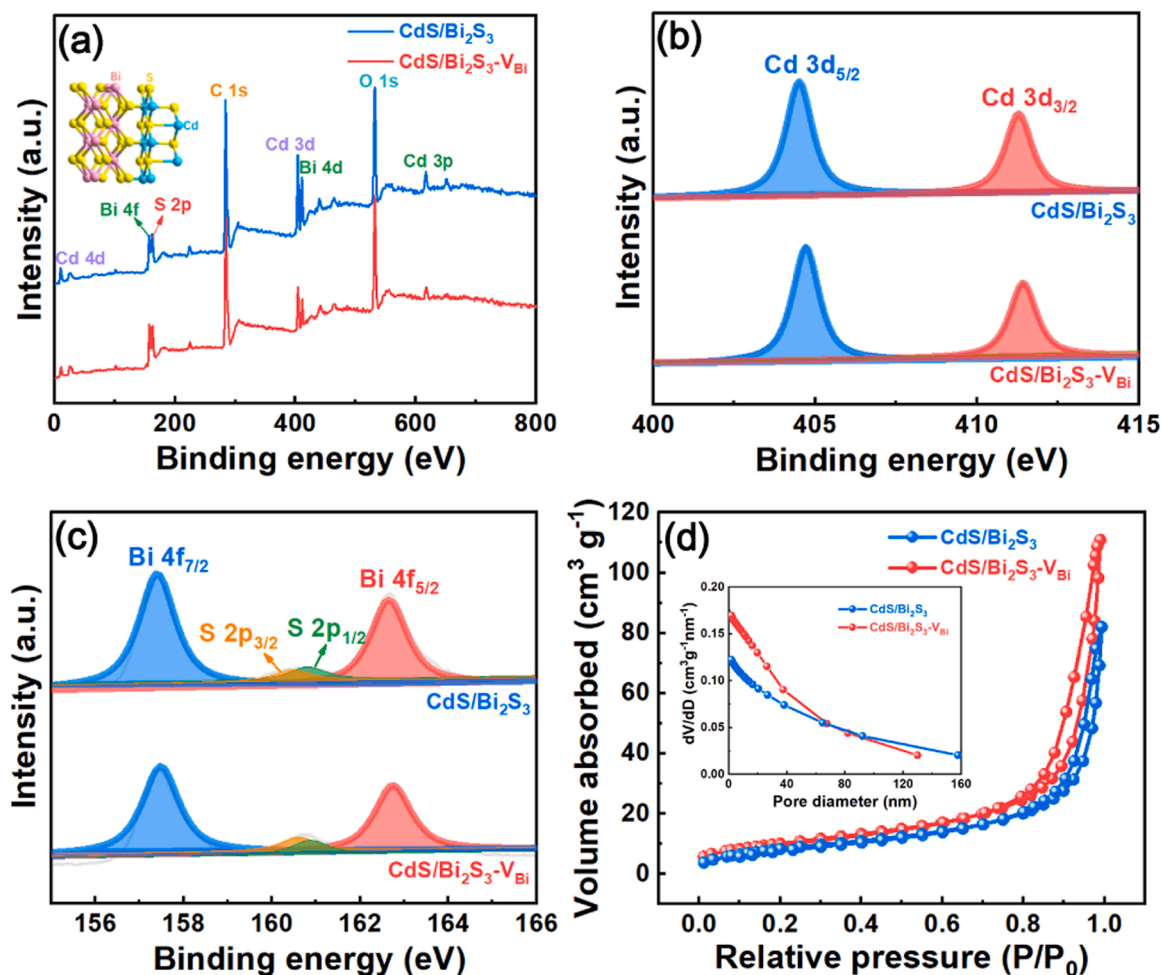Supplementary material related to this article can be found online at

Fig. 2. (a) XPS survey spectra of CdS/Bi_2S_3 and CdS/Bi_2S_3-V_{Bi} (The illustration is schematic diagram of CdS/Bi_2S_3 heterojunction structure). XPS spectra of CdS/Bi_2S_3 and CdS/Bi_2S_3-V_{Bi}: (b) Cd 3d, (c) Bi 4f and S 2p. (d) Nitrogen adsorption-desorption isotherm and pore-size distribution.

In order to verify the effect of magnetic field on carrier separation. The magnetic induction intensity are measured at different positions and heights of magnets by gauss meter. As shown in Fig. 3d–f, the vertical height of the magnet is 1.5 cm, and three diameter ranges (1 cm, 2 cm and 3 cm) are selected horizontally to measure the magnetic induction intensity of different magnets. Average the four points at the circle position in the magnet as shown in Fig. 3g. When the measured horizontal diameter is constant, the magnetic field strength increases in direct proportion to the number of magnets. When the horizontal measurement distance is 1 cm, the magnetic induction intensity changes from 711 Gs to 1182 Gs with the increase of the number of magnets. Fig. 3h–k demonstrates the magnetic induction intensity of different magnets when the height is measured at 2.5 cm. The horizontal measurement distance remains fixed, the distance of the magnet is inversely proportional to the magnetic induction intensity. According to Lorentz force formula $F = qvB$, the increase of magnetic intensity is beneficial to the enhancement of Lorentz force. The sonorous Lorentz force can effectively inhibit the recombination of carriers and improve the activity of photocatalytic hydrogen evolution.

The optical properties of the photocatalysts are explored by UV–vis-NIR diffuse reflectance spectroscopy (Fig. S5). Compared with CdS, the absorption intensity of CdS/Bi_2S_3 and CdS/Bi_2S_3-V_{Bi} are obviously enhanced, and the absorption edge are red-shifted. The above results show that the formation of heterojunction structure and Bi vacancy are beneficial to the absorption and utilization of light. Furthermore, Fig. S6 demonstrate the band gap of CdS is calculated to be 2.24 eV by the

Kubelka-Munk function ($\alpha h\nu = A(h\nu$-Eg). The band gap of Bi_2S_3 calculated is 1.53 eV. Based on the above experimental data, the relative positions of CdS and Bi_2S_3 energy levels can be obtained (Fig. S7).

The electron-hole recombination releases energy in the form of fluorescence, and the photoluminescence intensity represents the probability of electron-hole recombination. The weak fluorescence quenching of CdS/Bi_2S_3-V_{Bi} indicates that it has a low carrier recombination rate (Fig. S8). The bulk-carrier separation efficiency (η_{bulk}) of different samples is based on the research formula of Kim Group [37]. The η_{bulk} of CdS/Bi_2S_3-V_{Bi} under different magnetic field strengths are 13.6 %, 16.3 %, 29.8 % and 35.5 %, respectively (Fig. S9). The above experimental results show that the synergistic effect of negative magnetoresistance effect and Lorentz force can effectively inhibit charge recombination.

Electron paramagnetic resonance (EPR) spectroscopy is used to verify the direct pattern of electron behavior related to vacancies [38]. The characteristic peak at g = 2.006 indicates the existence of Bi vacancy in Bi_2S_3-V_{Bi} (Fig. 4a) [39,40]. The magnetic hysteresis loop of CdS, Bi_2S_3 and Bi_2S_3-V_{Bi} at room temperature is shown in Fig. 4b. Bi_2S_3-V_{Bi} hysteresis loops have typical ferromagnetic curves with small coercivity, it reaches saturation at a magnetic field of 14 kOe. According to quantum mechanics, the inherent magnetic moment of atoms is provided by unpaired electrons. The main source of magnetism is the electrons in the unfilled d or f shell of atoms. When corresponding to the ground state, the electronic shell structure of the sulfur atom state (neutral) is $1s^2 2s^2 2p^6 3s^2 3p^4$. In this case, the 3p orbital has the capacity to hold two electrons. The unfilled 3p orbitals can accept electrons from
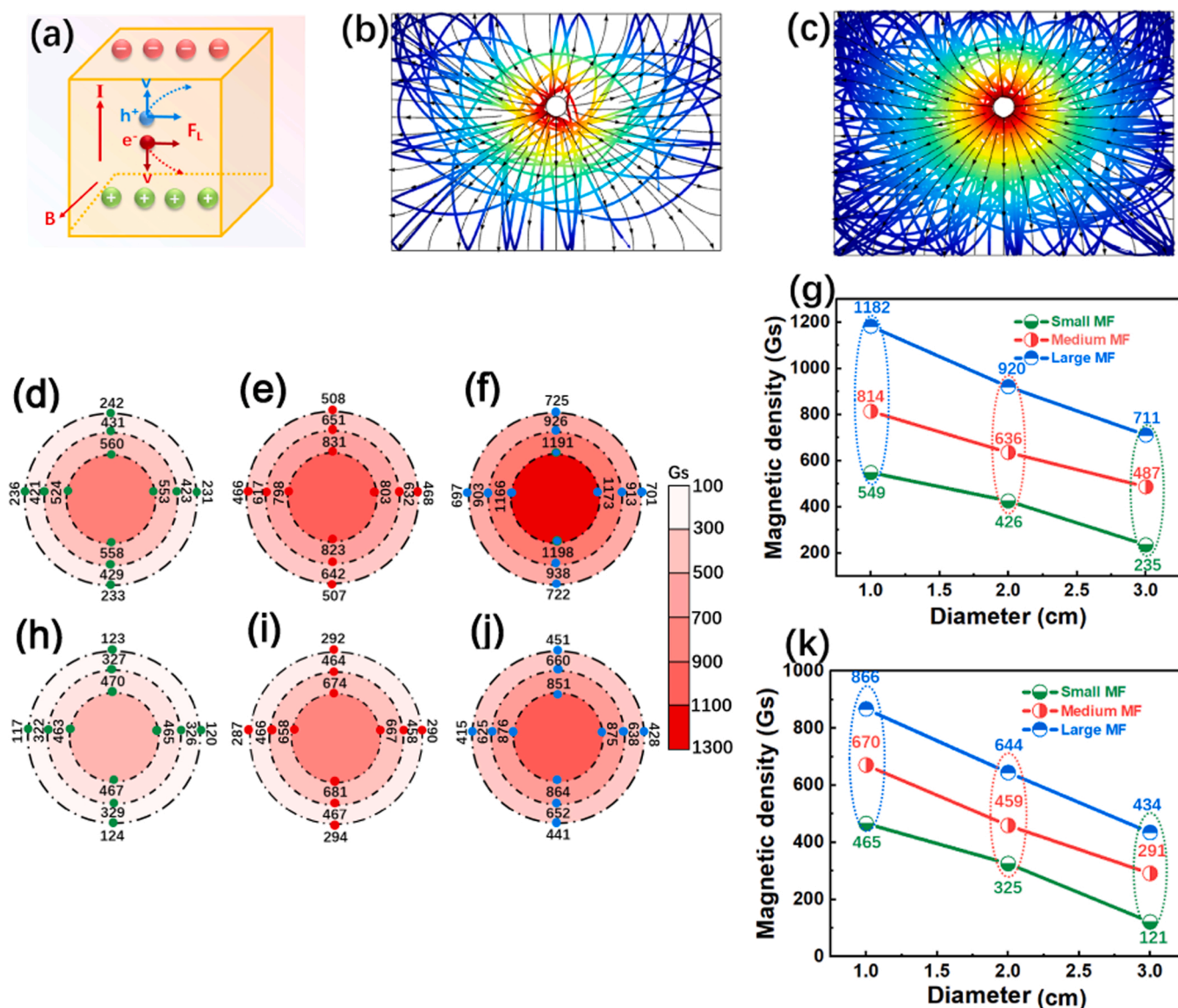
Fig. 3. (a) Schematic diagram of Lorentz force-induced carrier separation. (b, c) The trajectory of an electron in magnetic field. (d–g) Magnetic field intensity under different magnetic fields (Height = 1.5 cm, one magnet diameter = 3 cm, thickness = 0.5 cm). (h–k) Magnetic field intensity under different magnetic fields (Height = 2.5 cm).

adjacent bismuth atoms, and turn bismuth atoms and sulfur atoms into Bi^{3+} and S^{2-}. Its electronic shell structure becomes the closed shell $1s^2 2s^2 2p^6 3s^2 3p^6$. However, Bi^{3+} has no unpaired electrons in its d orbital when it forms, so Bi_2S_3 is nonmagnetic. In order to reasonably explain the influence of Bi vacancy on Bi_2S_3 magnetism, the first-principles calculation is used to discuss and analyze different dimensions. Fig. 4c,d show the optimized structure of Bi_2S_3-V_{Bi} in a direction and c direction. Its crystal has a layered structure, and each layered structure is a long atomic chain. Bi atoms and S atoms are bonded by covalent bonds. The layered structure extends infinitely along the (001) crystal plane direction. The adjacent layered structures are bonded by van der Waals force. In the differential charge diagram of Fig. 4e, yellow represents gain electron, and blue represents loss electron. The removed Bi atoms will bond with the surrounding S. From the size of the charge profile, it can be seen that the charge transfer between Bi and the lower two S atoms is greater than that between Bi and the upper two S atoms. This phenomenon will lead to a certain polarization, so that Bi_2S_3-V_{Bi} has a certain ferromagnetism. Fig. 4f exhibit the total spin state density of Bi_2S_3 and the partial spin state density of the P orbital of S atom and Bi atom. The results show that there is obvious spin

splitting near the Fermi level in the total density of states, which implies the existence of local magnetic moments. As shown in Fig. 4g, the enlarged illustration of PDOS shows that the spin splitting of Bi_2S_3-V_{Bi} mainly comes from the spin polarization of P electrons in S atoms, which leads to the magnetic moment generated by the system. As shown in Fig. S10, the enlarged P orbital of S atom and Bi atom state density diagram from 6 to 8 eV. The enlarged illustration of PDOS shows that the spin splitting of Bi_2S_3-V_{Bi} mainly comes from the spin polarization of P electrons in S atoms and Bi atoms. For the magnetism of Bi_2S_3 surface caused by vacancies, its magnetic moment is mainly distributed on the S atoms around the cation vacancies.

3.3. Characterization of negative magnetoresistance effect

Ferromagnetic materials consist of magnetic domains, which are atomic magnet groups formed by mutual effect or interchange coupling. The magnetic torque of atoms line up in the identical direction in separate domains, however, there are various directions in different fields. When a magnetic field is applied, the magnetic torque of atoms in different magnetic domains tend to arrange in the identical direction.
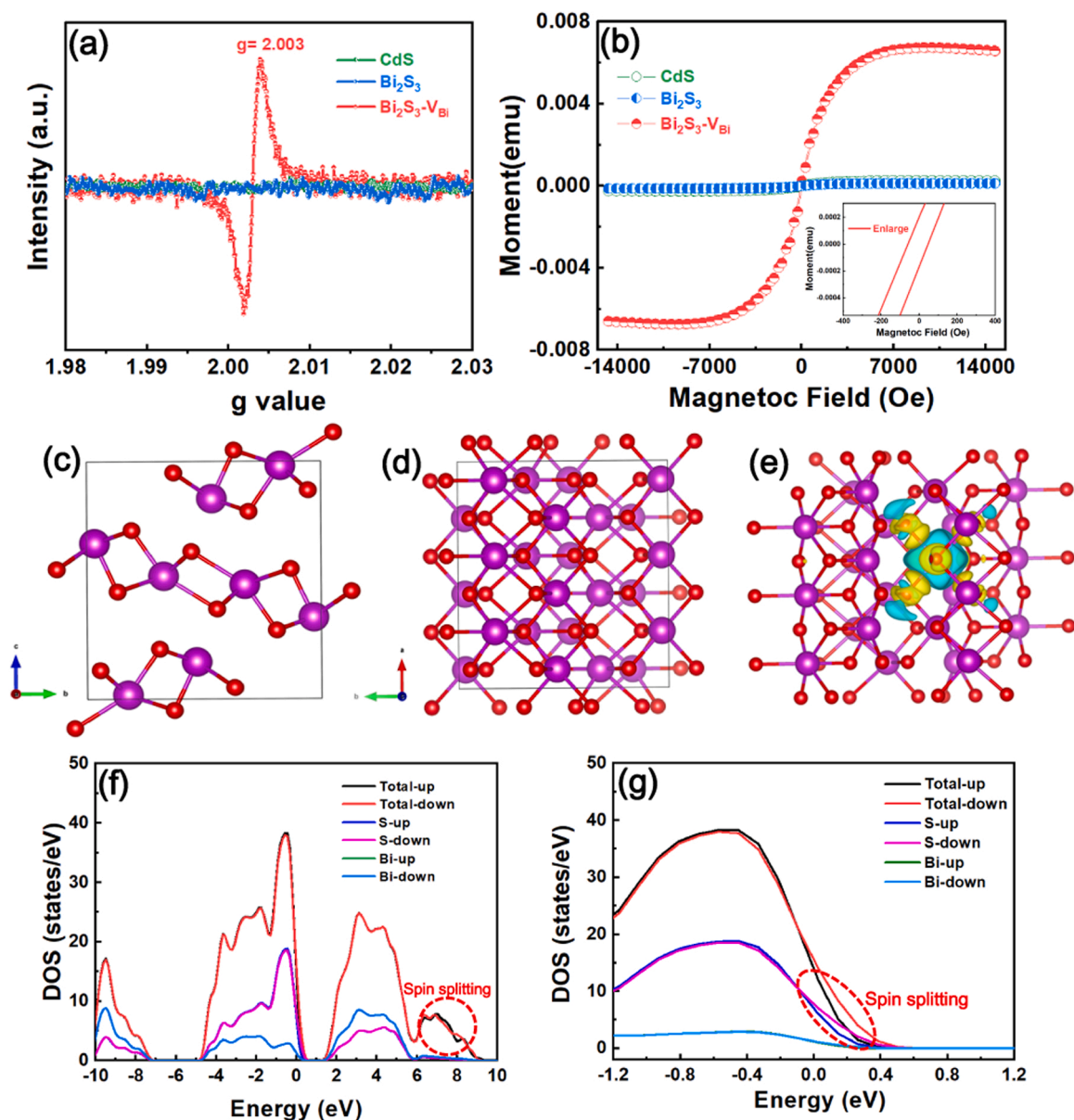
Fig. 4. (a) EPR spectra of Bi_2S_3 and Bi_2S_3-V_{Bi}. (b) Magnetic hysteresis loop of CdS, Bi_2S_3 and Bi_2S_3-V_{Bi} at room temperature. (c, d) Optimal geometry of Bi_2S_3-V_{Bi} in different directions. (e) The charge density difference of Bi_2S_3-V_{Bi}. (f, g) TDOS and PDOS of Bi_2S_3-V_{Bi}.

This arrangement rest with the intensity of the magnetic field, a process called magnetization (Fig. 5a). The magnetization will increase in direct proportion to the magnetic field until the saturation magnetization is achieved. The ferromagnetic Bi_2S_3-V_{Bi} has spin polarization under the action of external magnetic field. When the magnetic moments of adjacent ferromagnetic Bi_2S_3-V_{Bi} nanoparticles cannot be parallel to each other, the electrons that keep the spin state will inevitably have an additional magnetic coupling energy during the tunneling process. Considering this magnetic exchange energy, the magnetoresistance can be expressed as [42,44]:

$$MR = \Delta\rho \Big/ \rho = -\frac{JP}{4K_BT}\frac{M^2(H) - M^2(0)}{M_s^2}$$

where J is the exchange constant between Bi_2S_3-V_{Bi} nanoparticles, ρ is the electron polarization energy, M is the magnetization of the sample at a certain temperature and Ms is the saturation magnetization of the sample. The resistance drops rapidly with the rapid increase of magnetization. Because MR is negative, J is positive, indicating the existence of

antiferromagnetic inter-particle interaction.

Under the external field, the conduction electrons can realize the transition between particles through the tunneling of spin-polarized electrons [43,44]. The magnetic moment of randomly oriented particles can be changed by the external magnetic field, and the ferromagnetic arrangement of particles will reduce the resistivity and increase the tunneling of electrons [45,46]. It is called magnetization that the magnetic moments are aligned in the same direction to make a substance magnetic (Fig. 5b). Based on DFT theoretical calculation, the electrons on S-2p are spin-polarized at Fermi level, which leads to the formation of spin-polarized carriers. These carriers tunnel through grain boundaries, so they can be transported between different grains. In this transmission process, the scattering of carriers on the border is closely connected with the magnetic torque direction of the magnetic domain. When an external magnetic field is introduced, the magnetic torque directions of contiguous magnetic domains transform from disorder to uniformity. The spin-dependent scattering of electrons is suppressed, which reduces the transmission resistance of Bi_2S_3-V_{Bi}. With the enhancement of external magnetic field, Bi_2S_3-V_{Bi} has more obvious negative magnetoresistance
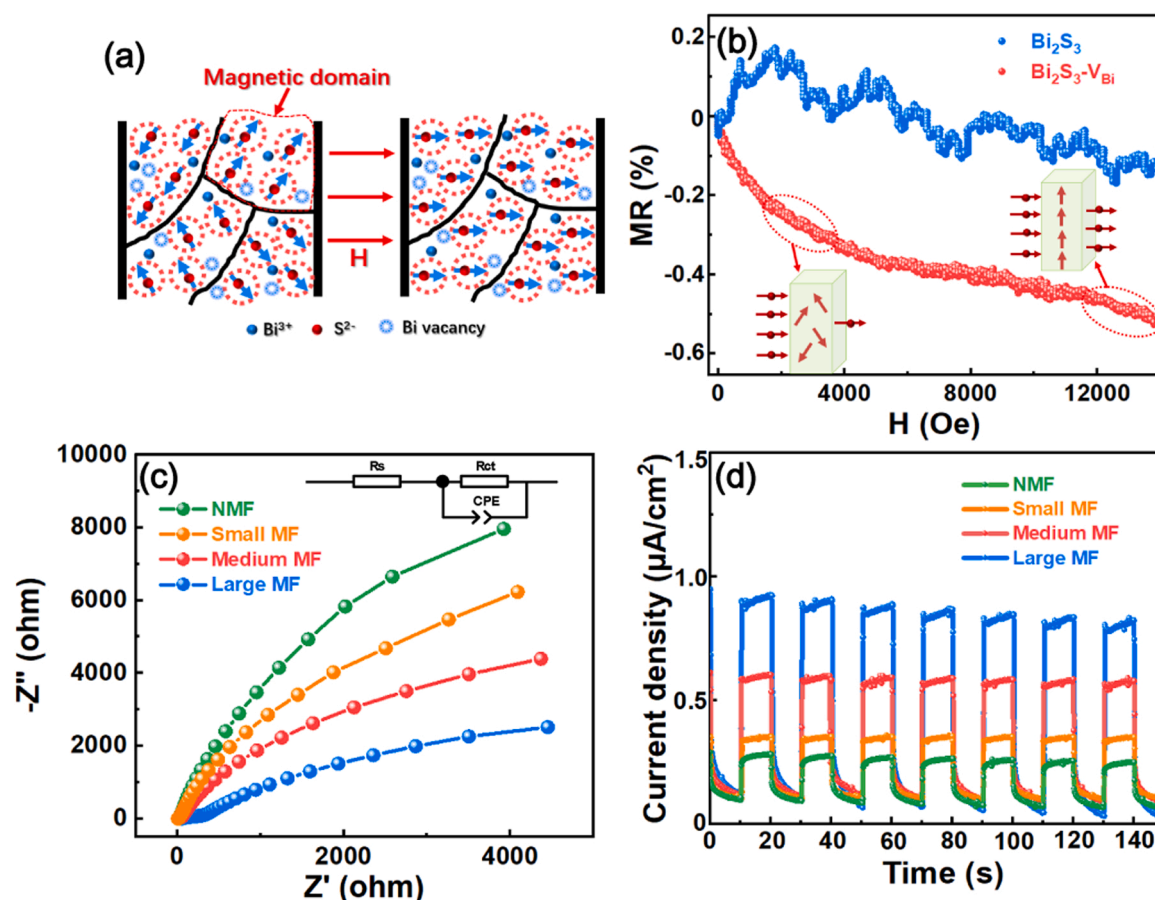
Fig. 5. (a) Mechanism diagram of electron spin state in magnetic field and non-magnetic field. (b) Magnetotransport properties of Bi_2S_3 and Bi_2S_3-V_{Bi} at room temperature. (c) Transient photocurrent and (d) electrochemical impedance spectroscopy plots of CdS/Bi_2S_3-V_{Bi} under different magnetic fields.

effect. This negative magnetoresistance effect caused by the spin polarization tunneling of the S-2p orbital causes more electrons to participate in the photocatalytic hydrogen evolution reaction.

The charge transfer ability and conductivity of photocatalyst are invested by electrochemical impedance spectroscopy (Fig. 5c). CdS/Bi_2S_3-V_{Bi} composites exhibit the largest arc radius and charge transfer resistance in the absence of magnetic field. In contrast, the circular radius decreases under large magnetic field, which effectively improves electron transfer efficiency. The above photochemical measurement results once again prove that the negative magnetoresistance effect of Bi_2S_3-V_{Bi} makes the carrier migration rate between CdS and Bi_2S_3-V_{Bi} faster. Furthermore, when electrons and holes recombine, Lorentz force acts on photocarriers and inhibits their recombination. The current density is directly related to the ability of carrier separation. Fig. 5d demonstrates the transient photocurrent response of CdS/Bi_2S_3-V_{Bi} composites under different magnetic fields. The photocurrent response of CdS/Bi_2S_3-V_{Bi} under large magnetic field is greater than that other conditions. In order to clearly distinguish the influence of Lorentz force and negative magnetoresistance effect on carrier separation, the transient photocurrent and electrochemical impedance spectra of pure CdS are measured under different magnetic fields. In the absence of negative magnetoresistance effect, the transient photocurrent and electrochemical impedance spectroscopy plots of pure CdS are shown in Fig. S11. CdS has smaller arc radius and larger photocurrent under large magnetic field. This result indicates that the carrier separation of photocatalyst is more favorable under larger magnetic field.

The separation and migration of photogenerated carriers are explored by photoelectrochemical measurement. As shown in Fig. S12a, the CdS/Bi_2S_3-V_{Bi} of linear scan voltammetry curve emerge lower hydrogen evolution potential under large magnetic fields.

Simultaneously, the Tafel slope is calculated based on linear scan voltammetry curve. Under the condition of increasing magnetic field, the Tafel slopes are 102 mV dec^{-1}, 85 mV dec^{-1}, 73 mV dec^{-1} and 58 mV dec^{-1}, respectively (Fig. S12b). The decreasing hydrogen evolution potential and the Tafel slopes indicate that CdS/Bi_2S_3-V_{Bi} has better photocatalytic reaction rate and performance under larger magnetic field conditions.

3.4. Photocatalytic hydrogen production performance

The hydrogen evolution efficiency of different photocatalysts in the absence of magnetic field is shown in Fig. 6a. The hydrogen production rate of CdS/Bi_2S_3 (2.35 mmol h^{-1} g^{-1}) is 2.14 times that of simple CdS (1.10 mmol h^{-1} g^{-1}). The reason for the increase of hydrogen production efficiency is that the built-in electric field generated provides driving force for the carriers separation. When Bi vacancy is introduced, the hydrogen production efficiency of CdS/Bi_2S_3-V_{Bi} (3.61 mmol h^{-1} g^{-1}) is obviously improved. This phenomenon is attributed to the negative magnetoresistance effect of Bi_2S_3-V_{Bi}, which promotes the rapid transfer of carriers and makes more electrons participate in the photocatalytic hydrogen evolution reaction.When the magnetic field is introduced into the photocatalytic reaction, the hydrogen evolution efficiency is obviously enhanced. The schematic diagram of photocatalytic reaction device is shown in Figs. S13a, S153 and S13c. Fig. 6b indicate that the hydrogen production efficiency of CdS, CdS/Bi_2S_3 and CdS/Bi_2S_3-V_{Bi}, under the condition of large magnetic field are 3.88 mmol $h^{-1}g^{-1}$, 5.50 mmol h^{-1} g^{-1} and 9.93 mmol h^{-1} g^{-1}, respectively. Meanwhile, the hydrogen production efficiency of CdS/Bi_2S_3-V_{Bi} are 5.69 mmol h^{-1} g^{-1} and 7.41 mmol h^{-1} g^{-1} under small and medium magnetic fields (Figs. S14 and S15). The reason for the
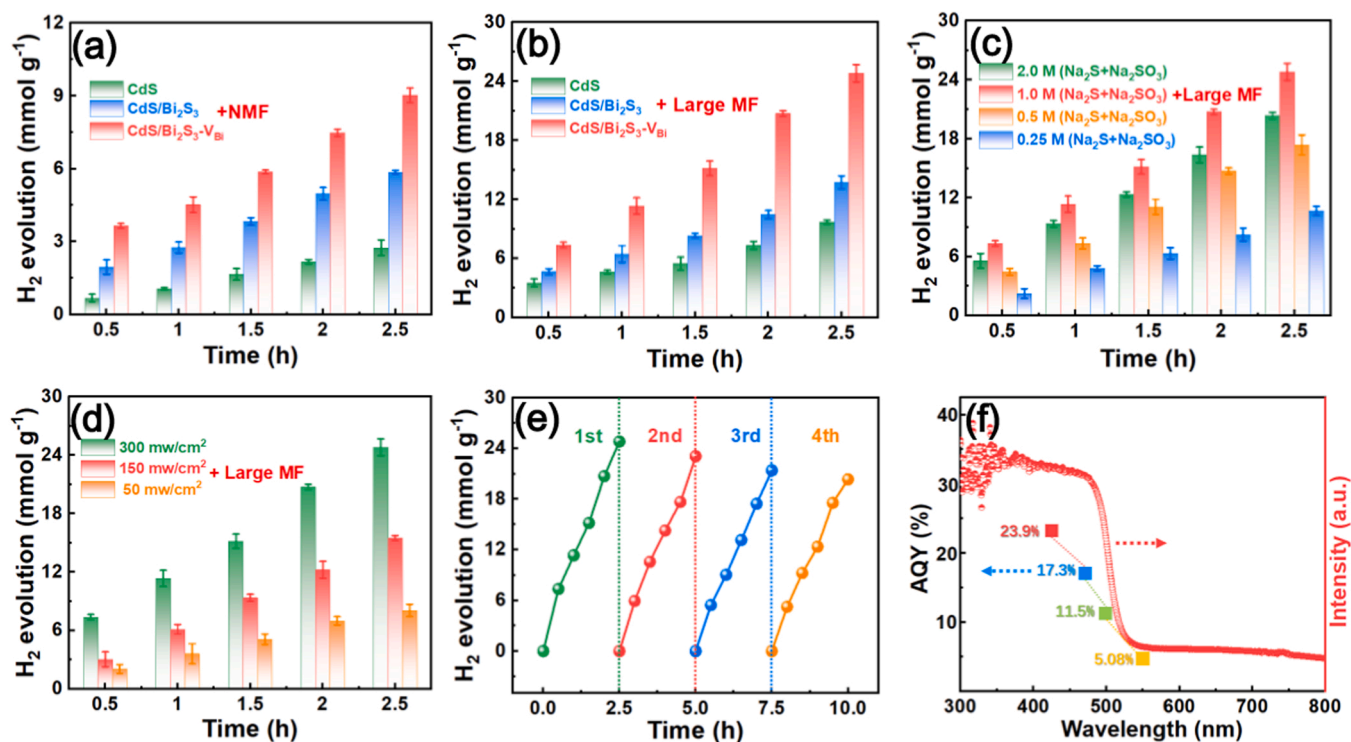
Fig. 6. The hydrogen evolution rate of CdS, CdS/Bi$_2$S$_3$ and CdS/Bi$_2$S$_3$-V$_{Bi}$ under (a) no magnetic field, (b) large magnetic field. The hydrogen evolution efficiency of CdS/Bi$_2$S$_3$-V$_{Bi}$ with (c) different concentrations sacrificial agents, (d) different power density under large magnetic field. (e) Cyclic stability of CdS/Bi$_2$S$_3$-V$_{Bi}$. (f) Fluorescence quantum yield of CdS/Bi$_2$S$_3$-V$_{Bi}$ at different wavelengths.

improvement of photocatalytic performance is that Lorentz force exerts opposite forces on electrons and holes. Thereby inhibiting the recombination of carriers and enabling more electrons to participate in the photocatalytic hydrogen evolution reaction. At the same time, the negative magnetoresistance effect caused by external magnetic field increases the carrier migration rate. Table S2 reveal the hydrogen evolution efficiency of heterojunction photocatalysts constructed by CdS in recent references. In addition, the hydrogen evolution efficiency of introducing magnetic field in photocatalytic reaction is shown in Table S3. Compared with previous literatures, the synergistic effect of negative magnetoresistance effect and Lorentz force is more beneficial to improve photocatalytic hydrogen evolution activity.

Sacrificial agent is used as electron donor to consume holes, thus inhibiting electron-hole recombination and increasing the lifetime of photogenerated electrons [43]. When the concentration of sacrificial agent is 0.25 M (Na$_2$S + Na$_2$SO$_3$), the hydrogen production efficiency of CdS/Bi$_2$S$_3$-V$_{Bi}$ is 4.27 mmol h^{-1} g^{-1} (Fig. 6c). With the increase of sacrificial agent concentration, the photocatalytic hydrogen production efficiency decreases gradually. This is mainly attribute to the sacrificial agent is oxidized into sulfur and attached to the surface layer of photocatalyst. This leads to the decrease of light utilization rate and covers the active sites of photocatalytic reaction. Fig. 6d shows the photocatalytic hydrogen evolution efficiency under different power densities. When the optical power density are 50 mW/cm^2, 150 mW/cm^2 and 300 mW/cm^2, the hydrogen evolution efficiency are 3.22 mmol h^{-1} g^{-1}, 6.19 mmol h^{-1} g^{-1} and 9.93 mmol h^{-1} g^{-1}, respectively. In the CdS/Bi$_2$S$_3$-V$_{Bi}$ composite photocatalyst, the conduction band electrons of Bi$_2$S$_3$-V$_{Bi}$ are transferred to CdS to reduce H*. However, since no incident light excites electrons on the valence band of the semiconductor photocatalyst, so that no hydrogen is generated. As shown in Fig. S16 and Table S4, the conclusion is consistent with the experimental results.

Cyclic stability of photocatalyst is particularly important for photocatalytic reaction. The hydrogen production performance of CdS/Bi$_2$S$_3$-V$_{Bi}$ composite photocatalyst has no apparent decrease after 10 h cycle

measurement (Fig. 6e). Meanwhile, Fig. S17 shows that the micromorphology of CdS/Bi$_2$S$_3$-V$_{Bi}$ after photocatalytic reaction has no obvious change, which indicates that CdS/Bi$_2$S$_3$-V$_{Bi}$ still has favorable cycle stability under the action of magnetic field. Fig. 6f shows the fluorescence quantum yields (AQY) of CdS/Bi$_2$S$_3$-V$_{Bi}$ at different wavelengths. The AQY measured at 425 nm, 475 nm, 500 nm and 550 nm are 23.9 %, 17.3 %, 11.5 % and 5.08 %, respectively, the variation trend of AQY is consistent with that of UV-Vis spectra.

3.5. Photocatalytic mechanism

The schematic diagram of carrier separation induced by the synergistic effect of negative magnetoresistance effect and Lorentz force is shown in Fig. 7. The realization of photocatalytic reaction requires semiconductor materials, but semiconductors with ferromagnetic properties are rare. Herein, Bi$_2$S$_3$-V$_{Bi}$ nanoparticles are ferromagnetic by introducing Bi vacancies. Under external magnetic field, the tunneling of spin-polarized electrons in S-2p orbit causes negative magnetoresistance effect. Therefore, more electrons in Bi$_2$S$_3$-V$_{Bi}$ can be transferred to CdS to participate in the photocatalytic hydrogen evolution reaction. At the same time, the semiconductor nanoparticles are affected by Lorentz force as they move perpendicular to the magnetic field. Lorentz force drives electrons and holes to move in opposite directions, thus inhibiting the rapid recombination of carriers. The synergistic effect of Lorentz force and negative magnetoresistance effect significantly improves the separation of carriers, and thus enhances the utilization rate of electrons in photocatalytic reaction.

4. Conclusions

In summary, the influence of external magnetic field on the performance of magnetic semiconductor photocatalyst is explored. In order to induce the ferromagnetism of semiconductor photocatalyst Bi$_2$S$_3$, the spin polarization of p electrons in S atoms is caused by introducing Bi
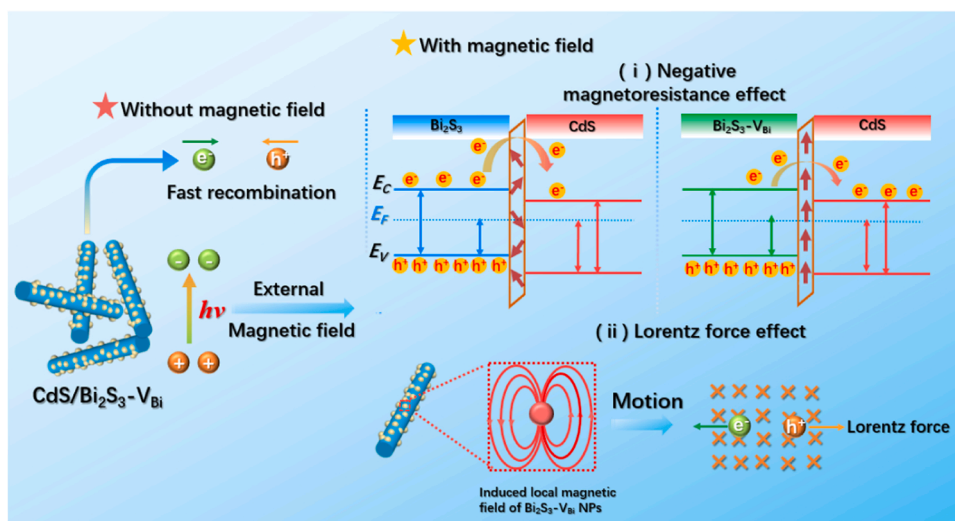
Fig. 7. Schematic diagram of photocatalytic reaction mechanism induced by negative magnetoresistance effect and Lorentz force.

vacancies. Under the action of external magnetic field, spin polarized electron tunneling in Bi_2S_3-V_{Bi} makes it have negative magnetoresistance effect. This is propitious to improve the effective transfer of carriers, thus fundamentally inhibiting the electron and hole recombination. Meanwhile, Lorentz forces act on photogenerated electrons and holes as the photocatalyst moves in the magnetic field. This makes the recombination of photo-generated carriers suppressed, and more electrons can participate in the photocatalytic reaction. The synergistic effect of Lorentz force and negative magnetoresistance effect makes further electrons participate in photocatalytic hydrogen evolution reaction. This study provides more possibilities for the application of magnetic field in the field of photocatalysis.

CRediT authorship contribution statement

Meng Li: Writing – original draft, Conceptualization, Methodology, Visualization, Investigation. **Jingxue Sun**: Writing – review & editing, Funding acquisition, Supervision. **Xin Zhou**: Supervision, Validation. **Huaisuo Yao**: Validation. **Bowen Cong**: Methodology. **Yingxuan Li:** Supervision. **Gang Chen**: Conceptualization.

Declaration of Competing Interest

The authors declare that they have no known competing financial interests or personal relationships that could have appeared to influence the work reported in this paper.

Data Availability

The authors are unable or have chosen not to specify which data has been used..

Acknowledgements

Appendix A. Supporting information

Supplementary data associated with this article can be found in the online version at doi:10.1016/j.apcatb.2022.122096.

References

[1] J.J. Qin, K.B. Chu, Y.P. Huang, X.M. Zhu, J. Hofkens, G.J. He, I.P. Parkin, F.L. Lai, T.X. Liu, The bionic sunflower: a bio-inspired autonomous light tracking photocatalytic system, Energy Environ. Sci. 14 (2021) 3931–3937.

[2] W. Xu, J. Wang, H. Yu, P. Liu, G.R. Zhang, H. Huang, D. Mei, Size-dependent electron injection over sensitized semiconductor heterojunctions for enhanced photocatalytic hydrogen production, Appl. Catal. B: Environ. 308 (2022) 121218–121225.

[3] F. Lin, S. Zhou, G. Wang, J. Wang, T. Gao, Y. Su, C.P. Wong, Electrostatic self-assembly combined with microwave hydrothermal strategy: construction of 1D/1D carbon nanofibers/crystalline g-C_3N_4 heterojunction for boosting photocatalytic hydrogen production, Nano Energy 99 (2022) 107432–107438.

[4] L.H. Lin, Z.Y. Yu, X.C. Wang, Crystalline carbon nitride semiconductors for photocatalytic water splitting, Angew. Chem. Int. Ed. 58 (2019) 6164–6175.

[5] Y.X. Zhao, L.R. Zheng, R. Shi, S. Zhang, X.N. Bian, F. Wu, X.Z. Cao, G.I. N. Waterhouse, T.R. Zhang, Alkali etching of layered double hydroxide nanosheets for enhanced photocatalytic N_2 reduction to NH_3, Adv. Energy Mater. 10 (2020) 2002199–2002208.

[6] S. Li, Z. Zhao, M. Liu, X. Liu, W. Huang, S. Sun, Y. Jiang, Y. Liu, J. Zhang, Z. Zhang, Remarkably enhanced photocatalytic performance of Au/AgNbO$_3$ heterostructures by coupling piezotronic with plasmonic effects, Nano Energy 95 (2022) 107031–107039.

[7] M. Li, J.X. Sun, B.W. Cong, S.Y. Yao, G. Chen, Sulphur vacancies modifed $Cd_{0.5}Zn_{0.5}S/Bi_2S_3$: engineering localized surface plasma resonance enhanced visible light driven hydrogen evolution, Chem. Eng. J. 415 (2021) 128868–128873.

[8] P. Ganguly, M. Harb, Z. Cao, L. Cavallo, A. Breen, S. Dervin, D.D. Dionysiou, S. C. Pillai, 2D nanomaterials for photocatalytic hydrogen production, ACS Energy Lett. 4 (2019) 1687–1709.

[9] Y.J. Yuan, D.Q. Chen, Z.T. Yu, Z.G. Zou, Cadmium sulfide-based nanomaterials for photocatalytic hydrogen production, J. Mater. Chem. A 6 (2018) 11606–11630.

[10] R.J. Feng, K.W. Wan, X.Y. Sui, N. Zhao, H.X. Li, X.F. Liu, X.H. Shi, L.R. Zheng, M. H. Liu, Anchoring single Pt atoms and black phosphorene dual co-catalysts on CdS nanospheres to boost visible-light photocatalytic H$_2$ evolution, Nano Today 37 (2021) 101080–101089.

[11] Y.T. Liu, M.Y. Lu, T.P. Perng, L.J. Chen, Plasmonic enhancement of hydrogen production by water splitting with CdS nanowires protected by metallic TiN overlayers as highly efficient photocatalysts, Nano Energy 89 (2021) 106407–106413.

[12] L. Shang, B.A. Tong, H.J. Yu, G.I.N. Waterhouse, C. Zhou, Y.F. Zhao, M. Tahir, L. Z. Wu, C.H. Tung, T.R. Zhang, CdS nanoparticle-decorated Cd nanosheets for efficient visible light-driven photocatalytic hydrogen evolution, Adv. Energy Mater. 6 (2016) 1501241–1501248.

[13] X.H. Zhang, Z.W. Chen, Y. Luo, X.L. Han, Q.Q. Jiang, T.F. Zhou, H.J. Yang, J.C. Hu, Construction of NH$_2$-MIL-125(Ti)/CdS Z-scheme heterojunction for efficient photocatalytic H$_2$ evolution, J. Hazard. Mater. 405 (2021) 2001529–2001536.

[14] X.Y. Lin, M.Y. Qi, Z.R. Tang, Y.J. Xu, Photochemical dehydrogenation of N-heterocycles over MOF-supported CdS nanoparticles with nickel modification, Appl. Catal. B: Environ. 317 (2022) 121708–121718.

[15] R.K. Chava, N. Son, M. Kang, Controllable oxygen doping and sulfur vacancies in one dimensional CdS nanorods for boosted hydrogen evolution reaction, J. Alloy. Compd. 873 (2021) 159797–159805.

[16] Y.J. Wang, J. Chen, L.M. Liu, X.X. Xi, Y.M. Li, Z.L. Geng, G.Y. Jiang, Z. Zhao, Novel metal doped carbon quantum dots/CdS composites for efficient photocatalytic hydrogen evolution, Nanoscale 11 (2019) 1618–1625.

[17] X.L. Yin, L.L. Li, M.L. Liu, D.C. Li, L. Shang, J.M. Dou, MoSx/CdS nano-heterostructures accurately constructed on the defects of CdS for efficient photocatalytic H₂ evolution under visible light irradiation, Chem. Eng. J. 370 (2019) 305–313.

[18] J. Zhang, X.B. Chen, Y. Bai, C. Li, Y. Gao, R.G. Li, C. Li, Boosting photocatalytic water splitting by tuning built-in electric field at phase junction, J. Mater. Chem. A 7 (2019) 10264–10272.

[19] L.L. Ling, Y.W. Feng, H. Li, Y. Chen, J.Y. Wen, J. Zhu, Z.F. Bian, Microwave induced surface enhanced pollutant adsorption and photocatalytic degradation on Ag/TiO₂, Appl. Surf. Sci. 483 (2019) 772–778.

[20] Y.W. Jiang, M.Z. Li, Y. Mi, L.Y. Guo, W.J. Fang, X.H. Zeng, T. Zhou, Y.S. Liu, The influence of piezoelectric effect on the heterogeneous photocatalytic hydrogen production of strontium titanate nanoparticles, Nano Energy 85 (2021) 105949–105957.

[21] M. Li, J.X. Sun, G. Chen, S.Y. Yao, B.W. Cong, P.F. Liu, Construction photothermal/pyroelectric property of hollow FeS₂/Bi₂S₃ nanostructure with enhanced full spectrum photocatalytic activity, Appl. Catal. B: Environ. 298 (2021) 120573–120579.

[22] J. Li, Q. Pei, R.Y. Wang, Y. Zhou, Z.M. Zhang, Q.Q. Cao, D.H. Wang, W.B. Mi, Y.W. Du, Enhanced photocatalytic performance through magnetic field boosting carrier transport, ACS Nano 12 (2018) 3351–3359.

[23] D. Sun, J. Mao, L. Cheng, X.L. Yang, H. Li, L.X. Zhang, W. Zhang, Q. Zhang, P.W. Li, Magnetic g-C₃N₄/NiFe₂O₄ composite with enhanced activity on photocatalytic disinfection of aspergillus flavus, Chem. Eng. J. 418 (2021) 129417–129422.

[24] Z. Zhao, D.D. Wang, R. Gao, G.B. Wen, M. Feng, G.X. Song, J.B. Zhu, D. Luo, H.Q. Tan, X. Ge, W. Zhang, Y.J. Zhang, L.R. Zheng, H.B. Li, Z.W. Chen, Magnetic field stimulated efficient photocatalytic N₂ fixation over defective BaTiO₃ perovskites, Angew. Chem. Int. Ed. 60 (2021) 11910–11918.

[25] Y. Zhang, L. Ran, Z. Li, P. Zhai, B. Zhang, Z. Fan, C. Wang, X. Zhang, J. Hou, L. Sun, Simultaneously efficient solar light harvesting and charge transfer of hollow octahedral Cu₂S/CdS p–n heterostructures for remarkable photocatalytic hydrogen generation, Trans. Tianjin Univ. 27 (2021) 348–357.

[26] F.Y. Du, Z. Lai, H.Y. Tang, H.Y. Wang, C.X. Zhao, Construction and application of BiOCl/Cu-doped Bi₂S₃ composites for highly efficient photocatalytic degradation of ciprofloxacin, Chemosphere (2021) 132391–132402.

[27] M. Zhang, S. Nie, T. Cheng, Y. Feng, C. Zhang, L. Zheng, L. Wu, W. Hao, Y. Ding, Enhancing the macroscopic polarization of CdS for piezo-photocatalytic water splitting, Nano Energy 90 (2021) 106635–106642.

[28] K. Zhou, W.L. He, X. Zhang, B. Zhang, X.N. Gong, K.W. Wang, Z.C. Zhang, X.L. Zhang, Z.N. Xia, X.Y. Zhou, Photocatalytic and photochemical processes of AgCl/TiO₂ studied with a fully integrated X-ray photoelectron spectrometer, Rare Met. 40 (2021) 799–807.

[29] M.S. Li, L.X. Zhong, W. Chen, Y.M. Huang, Z.X. Chen, D. Xiao, R. Zou, L. Chen, Q. Hao, Z.H. Liu, R.C. Sun, X.W. Peng, Regulating the electron-hole separation to promote selective oxidation of biomass using ZnS@Bi₂S₃ nanosheet catalyst, Appl. Catal. B: Environ. 292 (2021) 120180–120189.

[30] M. Solakidou, A. Giannakas, Y. Georgiou, N. Boukos, M. Louloudi, Y. Deligiannakis, Efficient photocatalytic water-splitting performance by ternary CdS/Pt-N-TiO₂ and CdS/Pt-N,F-TiO₂: interplay between CdS photo corrosion and TiO₂-dopping, Appl. Catal. B: Environ. 254 (2019) 194–205.

[31] J.K. Li, M. Li, Z.L. Jin, Rational design of a cobalt sulfide/bismuth sulfide S-scheme heterojunction for efficient photocatalytic hydrogen evolution, J. Colloid Interface Sci. 592 (2021) 237–248.

[32] Y. Li, X.M. Liu, L. Tan, Z.D. Cui, D.D. Jing, K.W.K. Yeung, D. Zheng, X.B. Wang, S.L. Wu, Eradicating multidrug-resistant bacteria rapidly using a multi functional g-C₃N₄@Bi₂S₃ nanorod heterojunction with or without antibiotics, Adv. Funct. Mater. 29 (2019) 1900946–1900962.

[33] L.Y. Shi, Z.L. Ma, W.W. Qu, W. Zhou, Z.Q. Deng, H.F. Zhang, Hierarchical Z-scheme Bi₂S₃/CdS heterojunction: controllable morphology and excellent photocatalytic antibacterial, Appl. Surf. Sci. 568 (2021) 150923–150931.

[34] Y.H. Ding, X.L. Zhang, N. Zhang, J.Y. Zhang, R. Zhang, Y.F. Liu, Y.Z. Fang, A visible-light driven Bi₂S₃@ZIF-8 core-shell heterostructure and synergistic photocatalysis mechanism, Dalton Trans. 47 (2018) 684–692.

[35] W.Q. Gao, J.B. Lu, S. Zhang, X.F. Zhang, Z.X. Wang, W. Qin, J.J. Wang, W.J. Zhou, H. Liu, Y.H. Sang, Suppressing photoinduced charge recombination via the Lorentz Force in a photocatalytic system, Adv. Sci. 6 (2019) 1901244–1901253.

[36] S.L. Zhang, W.W. Wang, D.M. Burn, H. Peng, H. Berger, A. Bauer, C. Pfleiderer, G. van der Laan, T. Hesjedal, Manipulation of skyrmion motion by magnetic field gradients, Nat. Commun. 9 (2018) 2115–2123.

[37] T.W. Kim, K.S. Choi, Nanoporous BiVO₄ photoanodes with dual-layer oxygen evolution catalysts for solar water splitting, Science 343 (2014) 990–994.

[38] S.Q. Zhou, Y.X. Zhao, R. Shi, Y.C. Wang, A. Ashok, F. Heraly, T.R. Zhang, J.Y. Yuan, Vacancy-rich MXene-immobilized Ni single atoms as a high-performance electrocatalyst for the hydrazine oxidation reaction, Adv. Mater. 34 (2022) 2204388–2204396.

[39] Y. Li, K. Xu, H. Hu, L. Jia, Y. Zhang, C. Zhuoga, P. Yang, X. Tan, W. Guo, W. Hao, T. Yu, J. Ye, Bi vacancy simultaneous manipulation of bulk adsorption and carrier utilization to replenish the mechanism of Cr(VI) photoreduction at universal pH, Chem. Eng. J. 450 (2022) 138106–138117.

[40] Y. Zhang, S. Gu, X.Y. Zhou, K.Y. Gao, K. Sun, D. Wu, J.J. Xia, X.F. Wang, Boosted photocatalytic nitrogen fixation by bismuth and oxygen vacancies in Bi₂MoO₆/BiOBr composite structures, Catal. Sci. Technol. 11 (2021) 4783–4792.

[42] J.G. Park, B.A. Collins, L.E. Darago, T. Runcevski, M.E. Ziebel, M.L. Aubrey, H.Z.H. Jiang, E. Velasquez, M.A. Green, J.D. Goodpaster, J.R. Long, Magnetic ordering through itinerant ferromagnetism in a metal-organic framework, Nat. Chem. 13 (2021) 594–602.

[43] T.X. Li, S.W. Jiang, N. Sivadas, Z.F. Wang, Y. Xu, D. Weber, J.E. Goldberger, K. Watanabe, T. Taniguchi, C.J. Fennie, K.F. Mak, J. Shan, Pressure-controlled interlayer magnetism in atomically thin CrI₃, Nat. Mater. 18 (2019) 1303–1309.

[44] Z. Shen, W. Zhang, S. Li, S. Mao, X. Wang, F. Chen, Y. Lu, Tuning the interfacial electronic conductivity by artificial electron tunneling barriers for practical lithium metal batteries, Nano Lett. 20 (2020) 6606–6613.

[45] H. Lin, Z.Y. Ma, J.W. Zhao, Y. Liu, J.Q. Chen, J.H. Wang, K.F. Wu, H.P. Jia, X.M. Zhang, H.X. Cao, X.X. Wang, X.Z. Fu, J.L. Long, Electric-field-mediated electron tunneling of supramolecular naphthalimide nanostructures for biomimetic H₂ production, Angew. Chem. Int. Ed. 60 (2021) 1235–1243.

[46] R. Guo, L.L. Tao, M. Li, Z.R. Liu, W.N. Lin, G.W. Zhou, X.X. Chen, L. Liu, X.B. Yan, H. Tian, E.Y. Tsymbal, J.S. Chen, Interface-engineered electron and hole tunneling, Sci. Adv. 7 (2021) 1033–1041.